Large-scale 3D inversion of marine magnetotelluric data: Case study from the Gemini prospect, Gulf of Mexico

Michael S. Zhdanov[1], Le Wan[1], Alexander Gribenko[1], Martin Čuma[1], Kerry Key[2], and Steven Constable[2]

ABSTRACT

Three-dimensional magnetotelluric (MT) inversion is an emerging technique for offshore hydrocarbon exploration. We have developed a new approach to the 3D inversion of MT data, based on the integral equation method. The Tikhonov regularization and physical constraint have been used to obtain a stable and reasonable solution of the inverse problem. The method is implemented in a fully parallel computer code. We have applied the developed method and software for the inversion of marine MT data collected by the Scripps Institution of Oceanography (SIO) in the Gemini prospect, Gulf of Mexico. The inversion domain was discretized into 1.6 million cells. It took nine hours to complete 51 iterations on the 832-processor cluster with a final misfit between the observed and predicted data of 6.2%. The inversion results reveal a resistive salt structure, which is confirmed by a comparison with the seismic data. These inversion results demonstrate that resistive geoelectrical structures like salt domes can be mapped with reasonable accuracy using the 3D inversion of marine MT data.

INTRODUCTION

Controlled-source electromagnetic (CSEM) and magnetotelluric (MT) techniques have become useful in oil and gas exploration offshore and in the deep-sea environment. The usefulness of marine EM methods in the search for hydrocarbons is based on the high resistivity of hydrocarbon-bearing layers and salt structures, both of which are typically surrounded by porous sediments saturated with conductive seawater. The CSEM method uses a dipole transmitter to create vertical loops of current that can be interrupted by the presence of thin resistive layers, making the CSEM method highly sensitive to hydrocarbon formations (e.g., Ellingsrud et al., 2002). However, the relatively narrow frequency range and strong attenuation of the CSEM dipole field limits the depth sensitivity of the CSEM method to only a few kilometers on the continental shelves.

The natural-source MT method uses a plane-wave electromagnetic field that diffuses into the seafloor, generating a predominantly horizontal current flow that is largely insensitive to thin horizontal resistive layers, but can be strongly perturbed by thicker resistive features such as salt structures (e.g., Constable et al., 1998; Hoversten et al., 1998). In addition, the much lower frequency range of MT data makes it a useful technique for mapping the resistivity of deeper structures, such as the decrease in porosity associated with basement formations (e.g., Key et al., 2006; Constable et al., 2009).

The reflection imaging technique, widely available and ever popular in exploration, can provide detailed images of the top of the salt surface, sedimentary layer, and basement formations. However, seismic imaging might not always provide sufficient details to interpret the salt base and nearby sedimentary structures. Common problems associated with salt include multiple reflections and mode conversions, the loss of reflected energy from steeply dipping salt surfaces, and the lack of coherent features beneath the salt structures.

Several publications present the results of marine MT surveys (Constable et al., 1998, 2009; Hoversten et al., 1998, 2000; Ellingsrud et al., 2002; Key, 2003; Key et al., 2006). In all of these publications, however, the interpretation of the sea-bottom MT data is based, as a rule, on 1D or 2D modeling, which limits the practical effectiveness of the MT method. The development of a truly 3D inversion method still represents a very challenging numerical and practical problem. The reasons are twofold. First, 3D forward modeling is a highly complicated and time-consuming mathematical problem in itself, especially for large-scale geoelectrical models. Second, the inversion of MT data is an unstable and nonunique problem. One should use regularization methods and physical constraints to obtain a stable and geologically meaningful solution of the inverse problem.

There exist several 3D MT inversion algorithms developed by different academic and industrial research groups. A review of the different MT methods can be found in Zhdanov (2009). In this paper, we introduce a method of rigorous 3D inversion of MT data, based on the integral equation (IE) method. We use the reweighted regularized conjugate gradient method (RRCG) for nonlinear MT inversion (Zhdanov, 2002). The main distinguishing feature of the RRCG algorithm is the application of the special stabilization functionals, which allow construction of smooth images of the underground geoelectrical structures and models with sharp geoelectrical boundaries. Although smooth solutions might be welcome in some inverse problems, geologic bodies with sharp boundaries often are more realistic. It is important also to be able to recover the boundaries of geologic features because drilling is expensive, and it is best to reduce the error rate as much as possible. One of the methods of the so-called focusing inversion involves a special kind of stabilizer, the minimum-support (MS) or minimum-gradient-support (MGS) stabilizers.

The method of regularized focusing inversion of the MT data is implemented in a new fully parallelized version of the computer code, which can be run on a PC cluster. One distinguishing feature of the new method and computer code is the possibility of taking into account the effect of sea-bottom bathymetry in the inversion of MT data. This is a very important problem in marine EM geophysics because the effect of sea-bottom bathymetry can significantly distort the useful MT response from subsea-bottom geoelectrical structures, which are the main target of offshore MT surveys (e.g., Key, 2003; Constable et al., 2009).

We apply the developed method to the interpretation of MT data collected by the Scripps Institution of Oceanography in the Gemini prospect, Gulf of Mexico. The main objective of this study is to demonstrate the capability of imaging a sea-bottom resistivity structure based on large-scale 3D inversion of marine MT data.

MT INVERSION METHOD AND ALGORITHM

Principles of regularized MT data inversion

In the MT method, the earth's natural electromagnetic field is used as a source field. The observed MT data are represented in the form of the impedance tensor in a Cartesian coordinate system (Berdichevsky and Dmitriev, 2002):

$$Z = \begin{bmatrix} Z_{xx} & Z_{xy} \\ Z_{yx} & Z_{yy} \end{bmatrix}. \tag{1}$$

The observed impedances are independent of the strength of the source. They depend only on the frequency of the signal and the electrical conductivity of the subsurface earth. The MT inversion is carried out commonly for the principal impedances Z_{xy} and Z_{yx}. However, the full impedance tensor provides more information about the subsurface structures.

We can describe the discrete magnetotelluric inverse problem by an operator equation:

$$\mathbf{d} = \mathbf{A(m)}, \tag{2}$$

where $\mathbf{d}$ stands for a data vector formed by the components of the impedances, $\mathbf{A}$ is the nonlinear forward operator symbolizing the governing equations of the MT modeling, and $\mathbf{m} = \Delta\sigma$ is a vector formed by an unknown set of anomalous conductivity (model parameters) within the targeted domain. The details of how to compute impedances (the data $\mathbf{d}$) from a nonlinear operator ($\mathbf{A}$) acting on

anomalous conductivity can be found in Zhdanov (2009). For example, if anomalous conductivity is equal to zero, then the observed data are the MT impedances for the background geoelectrical model.

We use the integral equation method (Hursán and Zhdanov, 2002; Zhdanov, 2002) for numerical calculation of the forward modeling operator in equation 2.

We apply the Tikhonov regularization to solve the inverse problem 2. It is based on minimization of the Tikhonov parametric functional:

$$P(\Delta\sigma) = \varphi(\Delta\sigma) + \alpha s(\Delta\sigma) = \min, \tag{3}$$

where

$$\varphi(\Delta\sigma) = \|\mathbf{W}_d[\mathbf{A}(\Delta\sigma) - \mathbf{d}]\|_{\ell_2}^2 \tag{4}$$

is the misfit functional between the predicted data $\mathbf{A}(\Delta\sigma)$ and the observed data $\mathbf{d}$, and $s(\Delta\sigma)$ is a stabilizing functional.

The main role of the stabilizing functional in the inversion process is to select the appropriate solution of the inverse problem from a class of models with assigned properties. Several possible choices exist for the stabilizer. We use three types of stabilizing functionals $s(\Delta\sigma)$: minimum-norm (MN), minimum-support (MS), and minimum-vertical-support (MVS) stabilizers (Gribenko and Zhdanov, 2007; Zhdanov et al., 2007; Zhdanov and Gribenko, 2008):

$$s(\Delta\sigma) = \begin{cases} s_{MN}(\Delta\sigma) = \beta_{MN}\|\mathbf{W}_m(\Delta\sigma - \Delta\sigma_{apr})\|_{\ell_2}^2 \\ s_{MS}(\Delta\sigma) = \beta_{MS}\|\mathbf{W}_e^{MS}\mathbf{W}_m\Delta\sigma\|_{\ell_2}^2 \\ s_{MVS}(\Delta\sigma) = \beta_{MVS}\|\mathbf{W}_e^{MVS}\mathbf{W}_m\Delta\sigma\|_{\ell_2}^2 \end{cases}. \tag{5}$$

These stabilizing functionals can be used separately or all together.

In equations 4 and 5, $\mathbf{W}_d$ and $\mathbf{W}_m$ are the data weighting matrix and model parameter weighting matrix; $\mathbf{W}_e^{MS}$ and $\mathbf{W}_e^{MVS}$ are focusing matrices (for a definition, see Zhdanov, 2002); α is a regularization parameter, and the $\Delta\sigma_{apr}$ term is a priori information about the anomalous conductivity model. The coefficients β_{MN}, β_{MS}, and β_{MVS} are called the minimum-norm, minimum-support, and minimum-vertical-support coefficients. These coefficients can be selected in the inversion process by the user, based on the nature of the problem and its required solution. In addition, a combination of the different stabilizers can be used in the inversion to emphasize the desirable features of the inverse model (e.g., a compact body and thin horizontal reservoir). The appropriate selection of the data weighting matrix ($\mathbf{W}_d$) and model-parameter weighting matrix ($\mathbf{W}_m$) are very important for the success of the inversion as well. We determine the data weights as a diagonal matrix formed by the inverse absolute values of the normal field. The computation of the model weighting matrix is based on sensitivity analysis (Zhdanov, 2002). As a result, we obtain a uniform sensitivity of the data to different model parameters.

In summary, the minimum-norm stabilizer selects the inverse model from the class of models with the least-squares norm. The minimum-support stabilizer ensures that the solution belongs to the class of models with the smallest domain of anomalous conductivity. The minimum-vertical-support stabilizer provides solutions for problems having the smallest vertical dimensions of the domain of anomalous conductivity.

The minimization problem 3 can be solved using any gradient-type technique. We use the regularized conjugate gradient (RCG)

method, which can be summarized as follows (Zhdanov, 2002):

$$\mathbf{R}_n = \mathbf{A}(\mathbf{m}) - \mathbf{d}$$

$$\mathbf{l}_n^{\alpha n} = \mathbf{l}^{\alpha n}(\mathbf{m}_n) = \mathbf{Re}(\mathbf{F}_n^* \mathbf{W}_d^2 \mathbf{R}_n) + \alpha \mathbf{W}_m^2 (\mathbf{m} - \mathbf{m}_{\mathrm{apr}})$$

$$\beta_n^{\alpha n} = \|\mathbf{l}_n^{\alpha n}\|^2 / \|\mathbf{l}_{n-1}^{\alpha n-1}\|^2$$

$$\widetilde{\mathbf{l}}_n^{\alpha n} = \mathbf{l}_n^{\alpha n} + \beta_n^{\alpha n} \widetilde{\mathbf{l}}_{n-1}^{\alpha n-1}$$

$$\widetilde{\mathbf{l}}_0^{\alpha 0} = \mathbf{l}_0^{\alpha 0}$$

$$k_n^{\alpha n} = (\widetilde{\mathbf{l}}_n^{\alpha n T} \mathbf{l}_n^{\alpha n}) / \{\|\mathbf{W}_d \mathbf{F}_{mn} \widetilde{\mathbf{l}}_n^{\alpha n}\|^2 + \alpha \|\mathbf{W}_m \widetilde{\mathbf{l}}_n^{\alpha n}\|^2\}$$

$$\mathbf{m}_{n+1} = \mathbf{m}_n - k_n^{\alpha n} \widetilde{\mathbf{l}}_n^{\alpha n}, \tag{6}$$

where $k_n^{\alpha n}$ is the step length, $\mathbf{l}_n^{\alpha n}$ is the gradient direction computed using an adjoint Fréchet derivative matrix $\mathbf{F}_n^*$, and α_n represents the subsequent values of the regularization parameter at the iteration number n.

The above inversion method is called an RCG scheme with adaptive regularization. It is based on the application of iterative algorithms of the minimization of the parametric functional. In the framework of the iterative approach, we begin the initial iteration without regularization ($\alpha_0 = 0$). We apply the regularization in the next step. The first value of the regularization parameter α_1 is determined after the initial iteration, as a ratio:

$$\alpha_1 = \frac{\|W_d \mathbf{A}(\mathbf{m}_0) - W_d \mathbf{d}\|^2}{\|W_m \mathbf{m}_0 - \mathbf{W}_m m_{\mathrm{apr}}\|^2}. \tag{7}$$

This selection of α_1 provides a balance between the misfit and stabilizing functional. For any subsequent iteration, we update the value of the regularization parameter α_k according to the progression

$$\alpha_k = \alpha_1 q^{k-1}, \quad k = 1,2,\ldots,n; \quad 0 < q < 1. \tag{8}$$

Coefficient q defines the rate of decrease of the regularization parameter. This coefficient usually is selected empirically by running several inversions with different q and evaluating the convergence plots versus the stability of inverse images. The iterative inversion is terminated when the misfit condition is reached:

$$\varphi(\mathbf{m}_{\alpha_{k0}}) = \|\mathbf{A}(\mathbf{m}_{\alpha_{k0}}) - \mathbf{d}\|^2 = \delta^2. \tag{9}$$

In the case of focusing inversion with minimum-support and minimum-vertical-support stabilizers, we use the reweighted regularized conjugate gradient method introduced in Zhdanov (2002, p. 161–166). The implementation details of the algorithm used for the Fréchet derivative calculations are specified in Zhdanov (2009, p. 637–645).

Memory allocation and matrix operation in parallel computing

We have implemented the inversion algorithm outlined above in the parallel computer code. The code has two modules: one for forward modeling and the other for inversion.

The forward modeling is based on the contraction integral equation (CIE) method (Hursán and Zhdanov, 2002). The system of linear equations of the CIE method can be written in the form

$$\mathbf{f} = \hat{\mathbf{L}} \mathbf{E}, \tag{10}$$

where $\mathbf{f}$ is a vector of the preconditioned background electric field, and $\mathbf{E}$ is a vector of the preconditioned total electric field in the anomalous conductivity domain.

We use the complex generalized minimal residual (CGMRM) method (Zhdanov, 2002) as a solver of the system of linear equations arising in the CIE method. This CGMRM algorithm ensures the convergence of the corresponding matrix inversion for arbitrary conductivity models.

The matrix $\hat{\mathbf{L}}$ of the forward operator 9 is formed by a product of the corresponding preconditioners and the matrix of the Green's tensor $\hat{\mathbf{G}}_D$ acting within the anomalous domain (Zhdanov, 2002). Hursán and Zhdanov (2002) show that if the anomalous domain is discretized into a horizontally homogeneous array of cells, the Green's matrix $\hat{\mathbf{G}}_D$ has a block Toeplitz structure. In this case, the number of different entries for storing matrix $\hat{\mathbf{G}}_D$ is much less than the total number of elements of the matrix, providing a good opportunity for economic storage. More specifically, the size of the Green's tensor kernels (the arrays storing all of the different matrix values) is $N_x \times N_y$ times smaller than the number of the elements in the original matrix. Here N_x and N_y stand for the number of cells in the x- and y-directions, respectively.

For example, if we discretize the anomalous body by a 20×20 grid in horizontal directions, the number of elements to be stored in the Green's tensor kernels is 400 times smaller than the size of the Green's matrix. Moreover, this property provides not only an economical storage, but an effective computational tool as well. It can be shown that the multiplication with the preconditioned matrix $\hat{\mathbf{L}}$ can be represented as a sequence of discrete 2D convolutions, followed by summation over the third (vertical) coordinate.

The matrix equation 9 can be written in scalar notations as

$$f_{\alpha i} = \sum_{\beta = x,y,z} \sum_{n=1}^{N_z} (\ell_{\alpha i \beta n} * E_{\beta n}), \quad \alpha = x,y,z; \quad i = 1,\ldots,N_z, \tag{11}$$

where $\ell_{\alpha i \beta n}$ is an array of matrix $\hat{\mathbf{L}}$ kernels (the array storing all different nonzero scalar components of $\hat{\mathbf{L}}$); α and β are the indices of the corresponding scalar components of the vector $\mathbf{E}$ (x-, y-, and z-components, respectively); i and n are the indices of the source and receiver positions along the vertical axis z in the expression for the Green's tensor; and the asterisk ($*$) denotes a discrete 2D convolution in the horizontal plane XY. We can apply the discrete convolution theorem

$$\ell_{\alpha i \beta n} * E_{\beta n} = FFT^{-1}[FFT(\ell_{\alpha i \beta n}) \cdot FFT(E_{\beta n})]. \tag{12}$$

The advantage of using this equation is that we replace the direct matrix multiplication with the fast Fourier transforms (FFTs), reducing the operational complexity from $O(N^2)$ to $O(N \log N)$, where $N = N_x \times N_y$.

The parallel computational libraries, however, generally are not suitable for the solution of this problem. We need to design the memory allocation model and the corresponding matrix operations to implement the fast Fourier transform algorithm on a distributed-memory machine, consisting of N processors and the same number of memory modules. Note that the parallel FFT is one of the most difficult operations, even in shared memory parallel architecture (Cvetanovic, 1987).

We use the 1D block cyclic distribution, which generally has a good memory access in the serial order in each process unit (PU),

and it provides fast computation for a large-scale problem (Black-ford et al., 1997). Figure 1 shows a simple example of our memory allocation in parallel with five process units (Yoshioka and Zhdanov, 2005). In this example, we assume that the domain with the anoma-lous conductivity is divided into $5 \times 3 \times 6$ cells in the x-, y-, and z-directions, respectively. Each PU holds the coefficients of the ma-trix equation for the corresponding layer as shown in Figure 1.

Note that the performance depends on the costs of the FFT and of the interprocessor communication. This balance can be changed by the optimization of the code, the size of the modeling grid, and the characteristics of the hardware. We have found that the cost of inter-processor communication is much more expensive than that of FFTs in this particular case.

The inversion part of the code, which takes considerably less time than the forward modeling, is parallelized over the vertical (Z) di-mension. The domain Z layers are distributed to the processors in se-quential order, each processor getting the number of Z layers equal to the total number of the Z layers in the inversion domain (N_z), divided by the number of processors (N_{proc}). All inversion data structures that span the inversion domain (model weights, domain conductivities, domain Fréchet derivatives, and so on) are distributed in this man-ner. Each processor holds in its memory and evaluates only the Z lay-ers that are assigned to it.

In the case of the Gemini model presented in this study, the inver-sion domain was discretized with $64Z$ layers. The inversion code was run on 64 processors, each of which calculated one Z layer. As there is a minimal intercell dependence in the evaluation of the in-version domain data, the inversion part of the code uses only a limit-ed amount of communication to calculate various L2 norms and to evaluate the minimization step length. The forward modeling part of the inversion code is parallelized in two levels: the higher level par-allelizes over the frequencies, the lower level over the product of Z layers and field components. The details of the lower level of paral-lelization were discussed above. The higher-level parallelization over frequencies is easy to implement, so it is just a matter of distrib-uting different frequencies on different sets of CPUs.
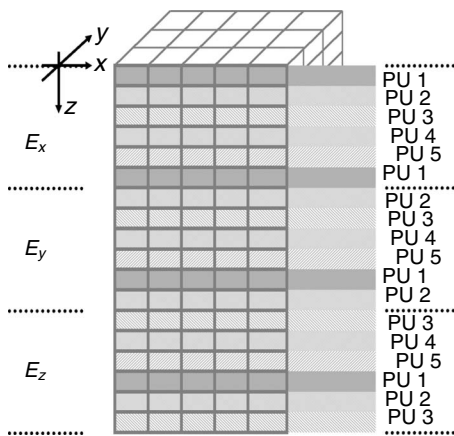

Figure 1. Memory model for the vector **E** allocation in the 1D block cyclic model. The figure shows the case of a forward modeling do-main divided into $5 \times 3 \times 6$ cells with five process units.

INVERSION OF MARINE MT DATA COLLECTED IN THE GEMINI PROSPECT, GULF OF MEXICO

Gemini prospect MT surveys

We tested this new 3D inversion capability by inverting broad-band MT data collected in a grid over the Gemini prospect, Gulf of Mexico (Key, 2003; Key et al., 2006). Located in 1-km-deep water about 200 km southeast of New Orleans, Gemini contains a salt body associated with a roho system that forced out salt both basin-ward and laterally, resulting in a complex 3D salt geometry (Schuster, 1995). High-resolution 3D seismic reflection data indi-cate that the salt resides between 1 and 5 km beneath the seafloor, al-though the deepest portions of the salt are not well resolved due to the lower fidelity of the deeper seismic data — some ambiguity ex-ists about whether the Gemini salt body is still rooted to the deeper Louann salt source layer or merely bottoms out at a depth of 5 to 6 km.

The existing knowledge of the salt body made Gemini an ideal test-bed location for the development of the Scripps Institution of Oceanography broadband marine MT instrument system (Constable et al., 1998). Surveys were carried out in 1997, 1998, 2001, and 2003, resulting in a grid of 42 broadband marine MT sites, as shown in Figure 2 (Key, 2003, Key et al., 2006).
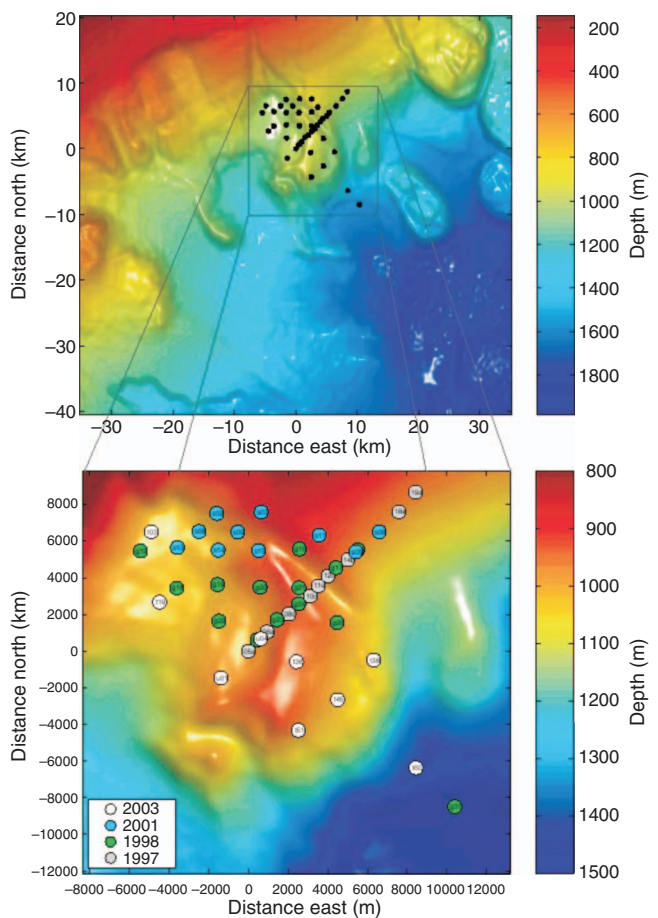

Figure 2. Bathymetry and MT site locations at the Gemini prospect. The MT sites are shown as circles with the color indicating the year the site was acquired.

Previous analysis of these data has been carried out on the profiles shown in Figure 3. Hoversten et al. (2000) examine 2D inversions of the densest profile (line A) and demonstrate that the marine MT can be effective for base-of-salt mapping. Key (2003) and Key et al. (2006) expand the 2D analysis to include all profiles and show that 2D inversions of certain MT data components can be used to effectively map some 3D sections of the salt. However, the finding is that, in strongly 3D regions, 2D inversion is insufficient for recovering the salt geometry.

One of the main difficulties in the 2D approach is related to the choice of the geoelectric strike direction, required in the framework of 2D inversion. In a general 2D approximation, a strike direction should exist in which conductivity does not vary significantly. However, in the case of the Gemini MT data, we have several mutually perpendicular lines, e.g., lines A and I. In this situation, an assumption that the conductivity does not change along a strike direction perpendicular to line A contradicts the fact that the observed data and the conductivity vary significantly along line I, and vice versa. A solution of this problem can be achieved by an application of the full 3D inversion method.

3D inversion of marine MT survey data

Three-dimensional inversion of the Gemini MT data was performed for all of the transect lines shown in Figure 3. The inversion domain was selected from −3 to 13 km and from −15 to 10 km in the horizontal x- and y-directions, and from 1 to 12 km in the vertical direction. The background geoelectrical model obtained by a 1D inversion consists of four layers: a seawater layer with a thickness of 1000 m and a resistivity of 0.33 ohm-m, a second sediment layer with a thickness of 7000 m and a resistivity of 1 ohm-m, and a third layer with a thickness of 4000 m and a resistivity of 5 ohm-m underlain by homogeneous sediments with a high resistivity of 60 ohm-m. The inversion domain was divided into $128 \times 200 \times 64 = 1,638,400$ cells with a cell size of 125×125 m in the x- and

y-directions and $50 \sim 500$ m in the vertical direction (the vertical size of the cells increases with the depth, varying from 50 to 500 m).

Figure 2 shows the bathymetry at the Gemini prospect, which varies from about 900 to 1500 m in the southeast corner of the survey area. The shape and conductivity contrast at the seafloor essentially make this boundary a large-scale 3D feature, which leads to local and regional distortions of the MT responses (e.g., Constable et al., 2009). Key (2003) finds that for a 1-ohm-m seafloor representative of Gemini, this seafloor terrain distortion is significant only at periods greater than 250 s. Previous 2D analysis circumvented this distortion by using only data at periods less than 250 s. For the 3D inversion carried out here, we account for terrain distortions by directly including seafloor bathymetry in the numerical grid and therefore consider the full 1- to 3000-s bandwidth of the MT responses. The bathymetry domain was extended from −3 to 13 km in the x-direction, from −15 to 10 km in the y-direction, and from 600 to 1500 m in the z-direction. The cell size was $250 \times 250 \times 25$ m. The bathymetry domain had $64 \times 100 \times 16 = 102,400$ cells.

The effect of the bathymetry on the MT data was incorporated in the inversion algorithm using the integral equation method with inhomogeneous background conductivity (IBC IE method) developed in Zhdanov et al. (2006). The IBC IE method is based on the separation of the effects due to excess electric current induced in the bathymetry domain, and those due to the anomalous electric current in the location of the anomalous conductivity, respectively. As a result, we arrive at a system of integral equations, which uses the same simple Green's functions for the layered model as in the original IE formulation. However, the new equations take into account the effect of the variable background conductivity distribution (Zhdanov, 2009).

To accomplish the inversion, we have used our newly developed parallel MT code that is capable of running on massively parallel supercomputers. For increased efficiency, the forward modeling part of the code uses two levels of parallelization. On the coarser level, we parallelize over the frequencies of the MT signal; on the finer level, we parallelize over the vertical dimension of the inversion domain. The inversion part, which takes considerably less time than the forward modeling, is parallelized just over the Z dimension of the inversion domain. The two-level parallelization was used over all 13 frequencies and over all 64Z layers, thus requiring $13 \times 64 = 832$ CPUs. We ran the inversion on the recently acquired Updraft cluster at the Center for High Performance Computing at the University of Utah. Updraft has 256 nodes connected with the Qlogic InfiniBand network. Each node includes eight Intel CPU cores running at 2.8 GHz and 16 GB of RAM. The inversion took nine hours to complete 50 smooth and 1 focusing iterations on the 832 processors and required 130 GB of disk space for intermediate files.

Figure 4 presents the convergence plot, which shows how the solution of the inverse problem converges in the adaptive iterative process. We plotted the normalized misfit, parametric functional, and regularization parameter versus iteration numbers. Note that we use adaptive regularization, which decreases the regularization coefficient at every iteration during which the parametric functional decreases according to formula 7. We should note that the apparently small values of the regularization parameter α, shown in the convergence plot, are compensated by the weights $\mathbf{W}_d$ and $\mathbf{W}_m$, which automatically provide a proper balance between the misfit and stabilizing functionals.
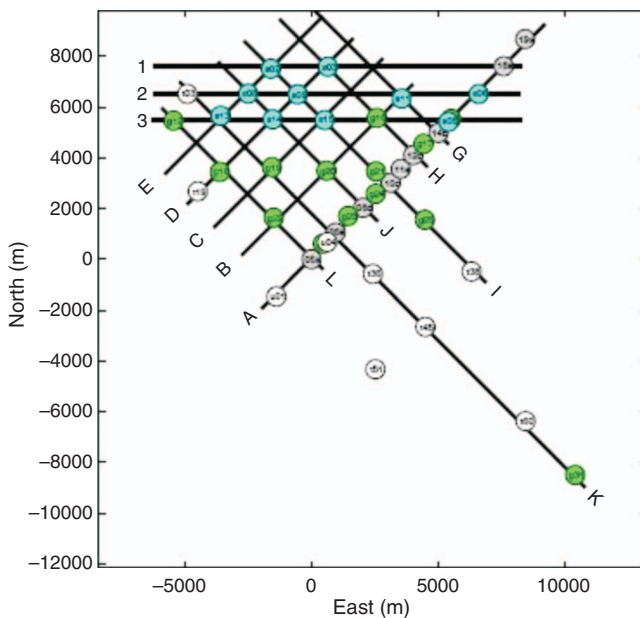

Figure 3. Location of MT profiles with the observation sites in the Gemini prospect, which were used in the 3D inversion (after Key, 2003).

Figure 4 shows a good convergence of the misfit and parametric functionals for this practical data set. We ran 50 iterations with the smooth minimum-norm stabilizer followed by 5 iterations with the focusing minimum-support stabilizer. However, we chose iteration
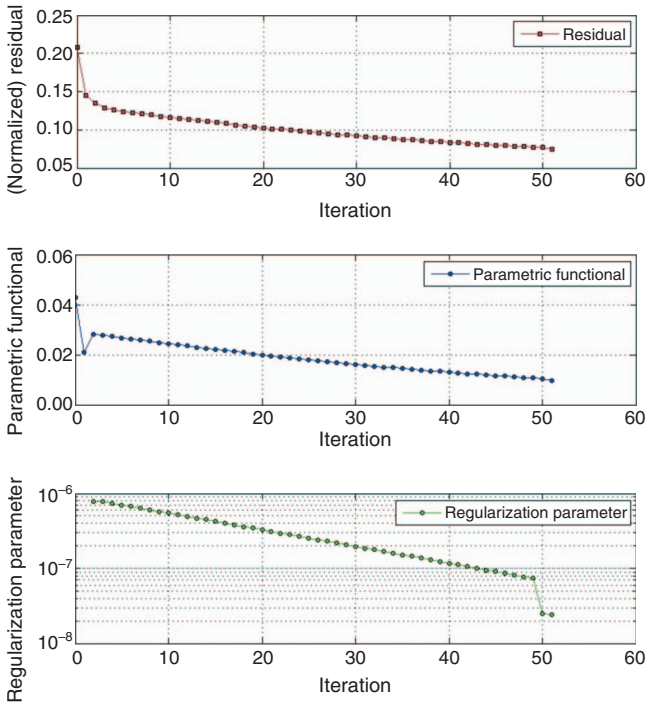

Figure 4. The plot shows the normalized misfit (difference between the observed and predicted data), parametric functional, and regularization parameter versus iteration number for 3D inversion of the MT data collected in the Gemini prospect, Gulf of Mexico.
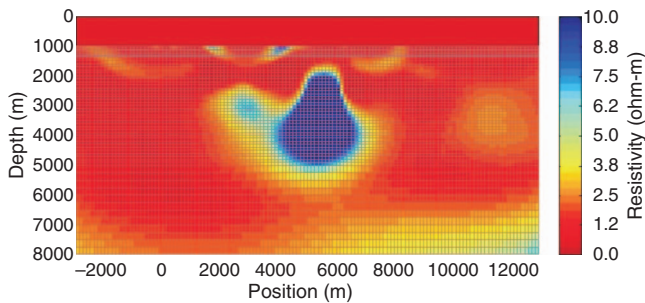
Figure 5. A vertical cross section of the 3D inversion results over line B.
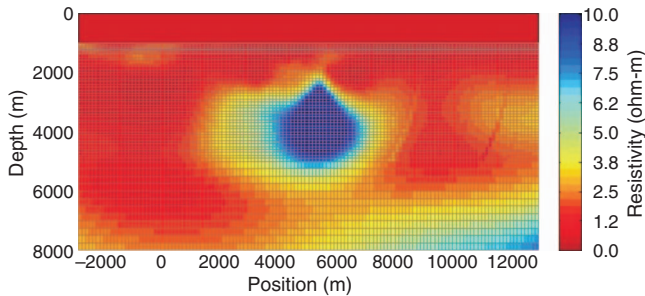
Figure 6. A vertical cross section of the 3D inversion results over line C.

51 as the final iteration because the misfit has leveled out after this iteration, reaching a level of 6.2%. Nevertheless, adding just one iteration with the focusing stabilizer helps to produce more contrast and focused image of the salt, as one could see from the images shown below. Note that the a priori delta sigma in the minimum-norm stabilizer was set to zero.

We present the vertical cross sections over lines A, B, C, and D in Figures 5–7. The 3D inverse model resolves very clearly the shape and location of the salt-dome structure, as determined using 3D seismic prestack depth migration. The vertical cross sections of the 3D inversion demonstrate reasonable recovery of the true geologic structure, particularly for the thick salt sections. The MT profiles show that thin deep salt is not resolved. Although some of this loss of resolution could arise from a lack of suitable data density and a relatively high noise level for this early experimental data, marine MT is known to have little sensitivity to salt that is much thinner than its depth of burial (e.g., Hoversten et al., 1998); this loss of resolution for thin deep salt is therefore expected. On the other hand, we can say with confidence that the salt in these regions must be thin because it is not recovered by the MT inversion.

A joint presentation of the MT inversion and seismic reflection data is shown for lines A and I in Figures 8 and 9. For line A, we see that the thick region of the salt is fairly well resolved, whereas the 1-km-thick portion that extends to the left at the 4-km depth is not resolved. For line I, the presence of the tabular salt body in the MT inversion correlates well with the lateral position of the seismic salt, whereas the top-salt and base-salt depths disagree by as many as 1 to 2 km. The 3D inversion for line I recovers the thin overhanging tongue of salt located at a horizontal position of 4 to 6 km and a depth of 2 to 3 km, which was identified in an earlier 2D inversion (Key et al., 2006).
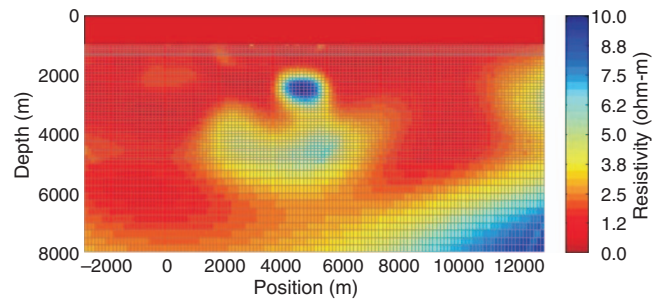

Figure 7. A vertical cross section of the 3D inversion results over line D.
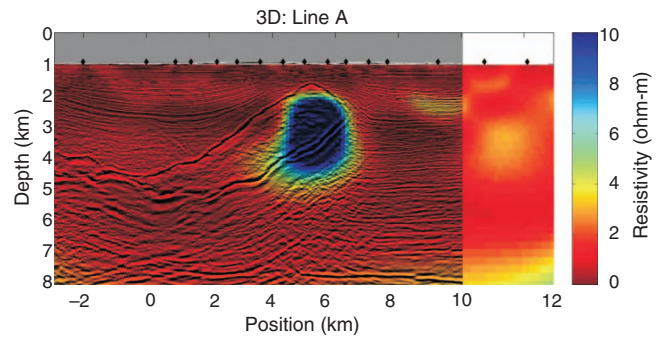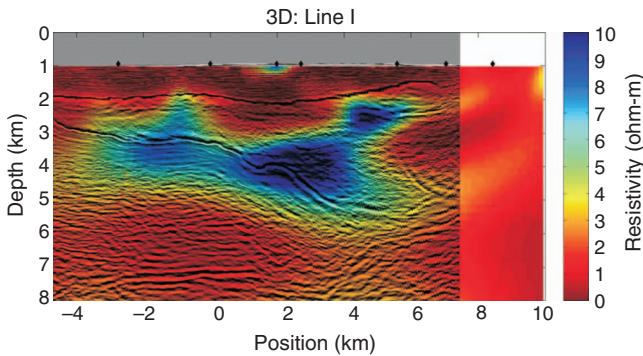

Figure 8. Line A: The combined 3D MT inversion results overlap with a seismic section representing depth-migrated reflections from the 3D seismic survey.
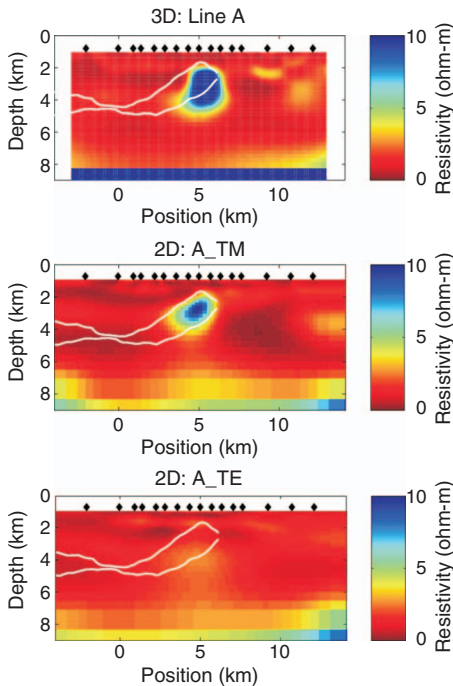
We point out that there is a good agreement in some places between the geoelectrical and seismic models of the salt boundaries, whereas in others there are discrepancies of as many as a few kilometers. Without having borehole data, it is difficult to decide whether such differences are caused by uncertainties in MT inversion or seismic interpretation. However, it is well known that it is difficult to resolve the accurate position of the resistive layer from the MT data. It is also hard to disentangle whether such disagreements arise from true structural differences or from a lack of suitable data coverage from these relatively sparse early marine MT test deployments in the Gemini prospect. Certainly some of the recent MT stations with modern receivers provide better quality data than the Gemini data. Thus, the results of this study should be treated as an illustration of the viability of large-scale 3D marine MT inversion for mapping salt, instead of being representative of the present state of the art in marine MT data collection and accuracy of mapping of the salt structure.

The quantitative analysis of the sensitivity of MT data to the salt structure is discussed in previous publications. For example, we could reference the papers by Key (2003) and Key et al. (2006), which present the extensive analysis of MT sensitivity and the plots of the MT data for the 2D model response and 3D seismic salt forward responses.

Figures 10–12 show a comparison along lines A, D, and H of the MT survey of the results obtained by 2D and 3D inversions. The top parts in these figures show the results of our 3D inversion, and the middle and bottom parts present the results of 2D TM- and TE-mode inversions obtained by Key (2003) and Key et al. (2006). The white
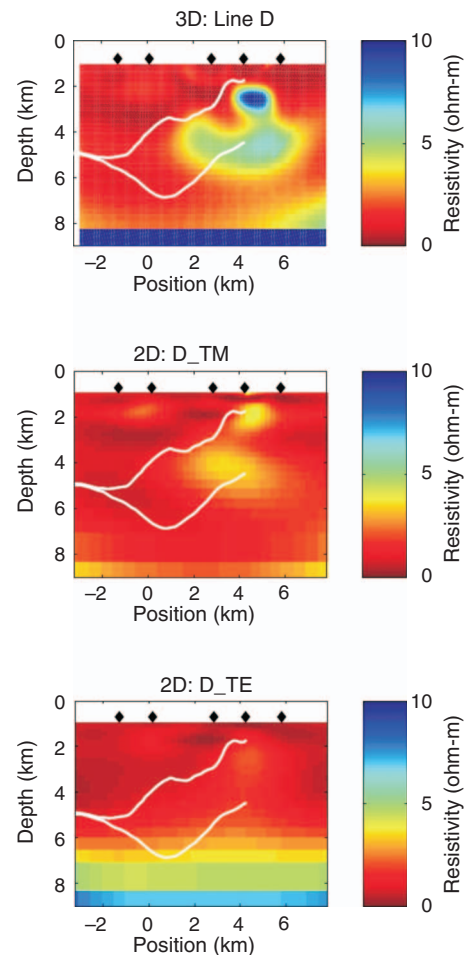

Figure 9. Line I: The combined 3D MT inversion results overlap with a seismic section representing depth-migrated reflections from the 3D seismic survey.

Figure 10. A comparison along line A of the MT survey of the results obtained by 2D and 3D inversions. The top part shows the results of full 3D inversion, the middle part presents the result of 2D inversion of the TM-mode data, and the bottom part shows a similar result of 2D inversion of the TE-mode data obtained by Key et al. (2006). The white contour indicates the position of the salt dome estimated on the basis of seismic reflection data.
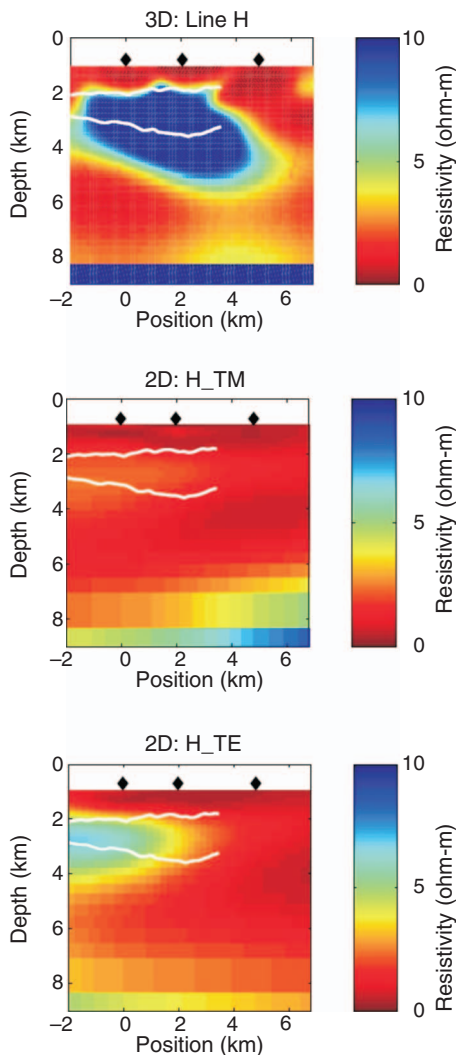

Figure 11. A comparison along line D of the MT survey of the results obtained by 2D and 3D inversions. The top part shows the results of full 3D inversion, the middle part presents the result of 2D inversion of the TM-mode data, and the bottom part shows a similar result of 2D inversion of the TE-mode data obtained by Key et al. (2006). The white contour indicates the position of the salt dome estimated on the basis of seismic reflection data.

contour indicates the position of the salt dome estimated on the basis of seismic reflection data. We note, however, that the seismic outline of the salt dome shown in Figures 10–12 can be used only for a qualitative comparison because it depends on a selection of the seismic wave velocity, which could not be done objectively in this area.

These qualitative comparisons show several important differences that reflect the superior capabilities of 3D inversion over 2D inversion. The inverse model for the TM mode in line A shows a salt-dome structure at the right depth with a resistivity of as much as 10 ohm-m. The inverse model for the TE mode contains a weak resistive anomaly slightly deeper than in the TM-mode image. The inverse geoelectrical model generated by the rigorous 3D inversion shows a strong resistivity anomaly at the location of the salt dome, which extends slightly deeper than the TM-mode anomaly, approximately to the depth of the weak anomaly shown in the TE-mode inverse model. The situation is different for lines D and H, at which 2D

inverse models show a very weak anomaly at the location of the salt dome, whereas 3D inversion still shows a resistive body at this depth (Figures 11 and 12). It is clearly seen from a comparison between 2D and 3D inverse images that 3D focusing inversion generates a much stronger resistivity contrast than smooth 2D inversion.

We observe also that the resistivity of salt recovered by 3D inversion is about 10 ohm-m. Similar results were obtained by other researchers (e.g., Hoversten et al., 2000; Key et al., 2006). This result is justified because the "MT response saturates as the resistivity of a body becomes greater than 10–20 times that of the background. In the GOM [Gulf of Mexico], bulk salt resistivities are more than 20 times the background sediment resistivities and, for the skin depths of interest, the MT response is totally governed by the distortion of electric currents in the sediments around the resistive salt" (Hoversten et al., 2000, p. 1482). The saturation of the MT response for resistive layers is well known by MT practitioners. It is easy to demonstrate, for example, that for a 1-km-thick resistive layer buried 1 km deep in 1-ohm sediments (somewhat similar to the Gemini salt), the difference between 10- and 100-ohm-m resistivities for the layer yields no appreciable differences in the MT response; hence the response has become saturated. The difficulty to resolve thin salt at a 4-km depth logically follows from this as well.

We present in Figure 13 a 3D view of the geoelectrical inverse model and the bathymetry in the area of the survey. One can clearly see the location and shape of the salt-dome structure in all of these images.

Figures 14 and 15 present comparisons between the observed and predicted data (in the form of apparent resistivity and phase, respectively) for the XY and YX polarizations at frequencies of 0.039, 0.63, 0.1, and 0.25 Hz. From the observed and predicted maps for the XY and YX polarizations, one can see a good match between the observed and predicted data shown in Figures 14 and 15. The limited length of this paper does not allow us to include the multiple figures illustrating the misfit distribution in space and with frequencies. However, we did not observe any specific pattern in the misfit behavior.

Figure 12. A comparison along line H of the MT survey of the results obtained by 2D and 3D inversions. The top part shows the results of full 3D inversion, the middle part presents the result of 2D inversion of the TM-mode data, and the bottom part shows a similar result of 2D inversion of the TE-mode data obtained by Key et al. (2006). The white contour indicates the position of the salt dome estimated on the basis of seismic reflection data.
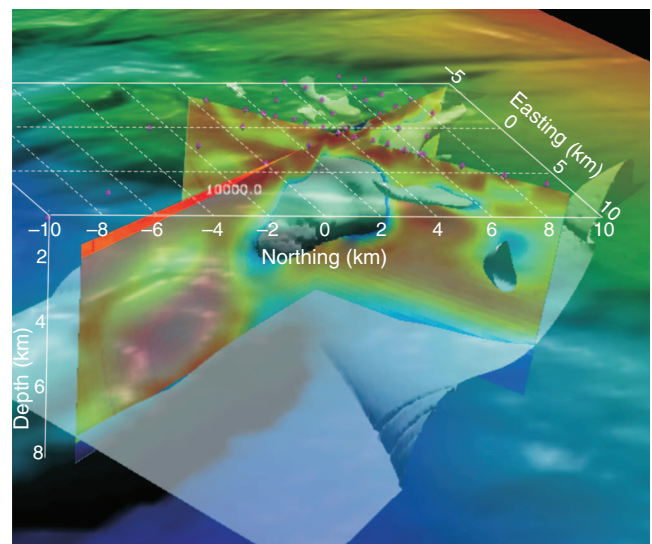

Figure 13. A 3D image of the inversion result for the Gemini prospect MT data in the presence of the sea-bottom bathymetry.
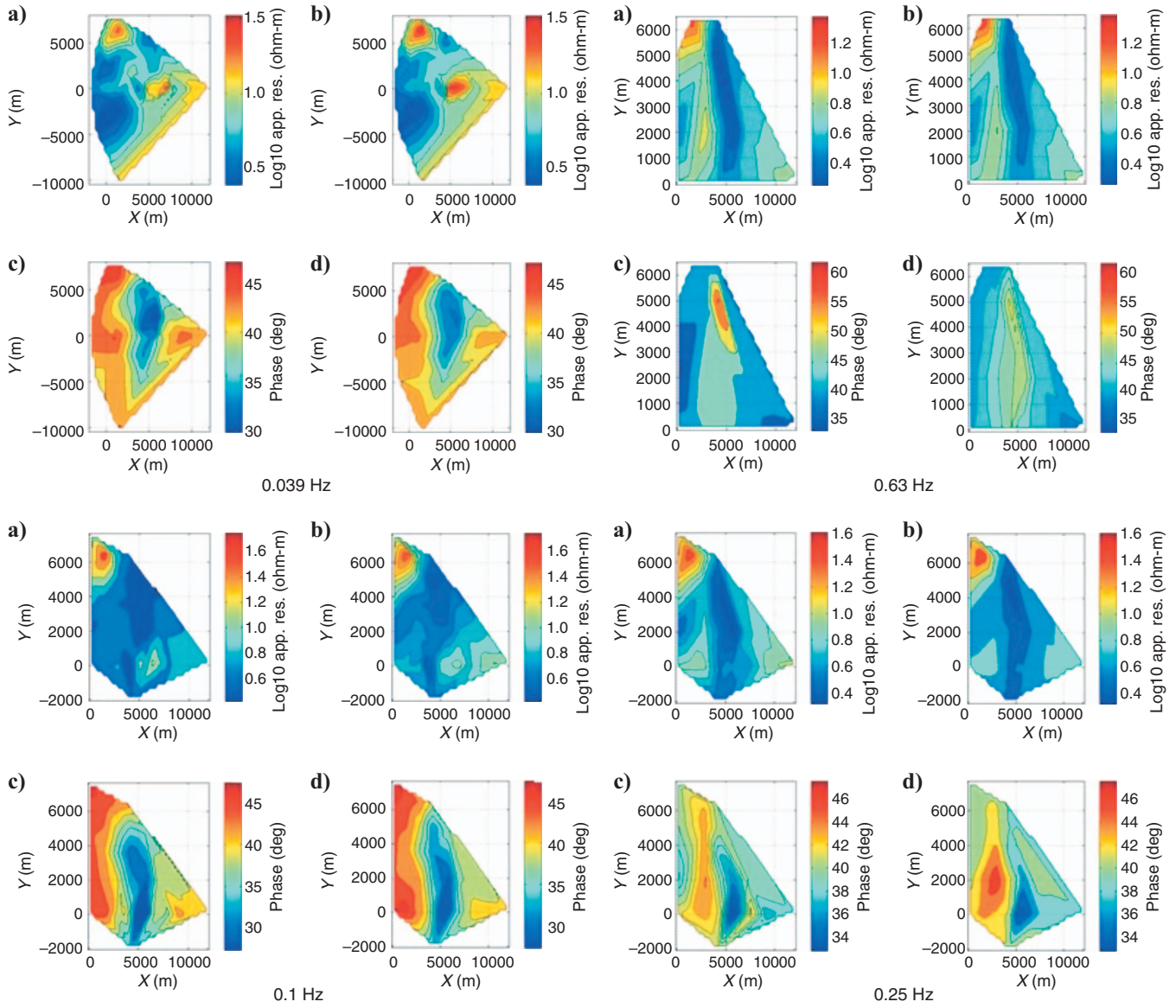
Figure 14. Maps of (a, b) observed and predicted apparent resistivity, and (c, d) observed and predicted phase, for *XY* polarization at frequencies of 0.039, 0.063, 0.1, and 0.25 Hz.
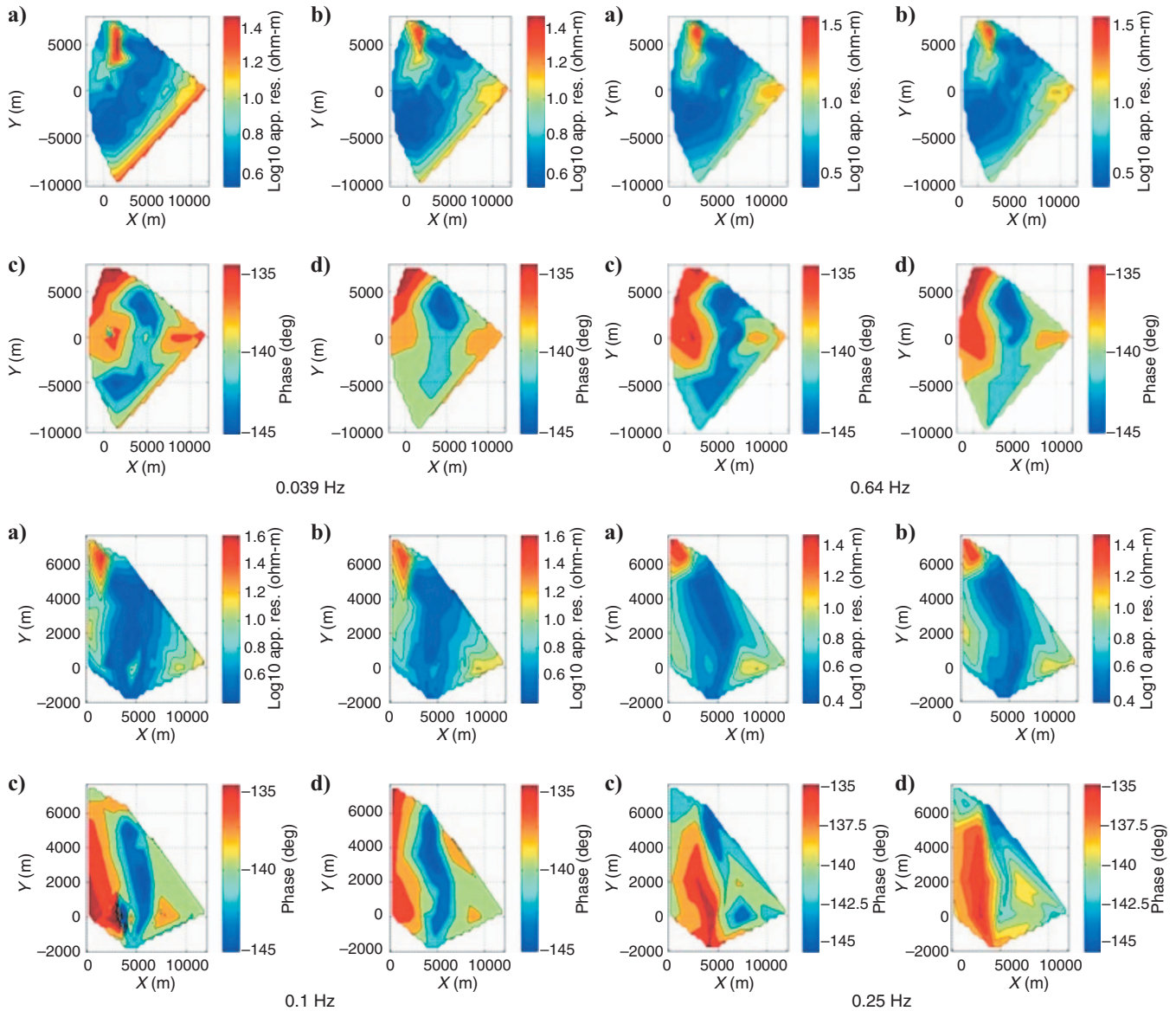
Figure 15. Maps of (a, b) observed and predicted apparent resistivity, and (c, d) observed and predicted phase, for *YX* polarization at frequencies of 0.039, 0.063, 0.1, and 0.25 Hz.

CONCLUSIONS

We have developed and analyzed a new version of the 3D inversion algorithm for the interpretation of MT data. This new algorithm is based on the IE method. It uses different focusing stabilizing functionals, which allow us to produce stable and focused structures of a geoelectrical target in an offshore environment. The new algorithm can take into account the effect of sea-bottom bathymetry on the observed MT data. The method is fully parallelized and can be run on a PC cluster.

We have applied this inversion method for the interpretation of field MT data collected in the Gemini prospect, Gulf of Mexico. The inversion for almost 1.6 million discretization cells took only nine hours on the 832 processors and required 130 GB of disk space for intermediate files. The obtained 3D inverse model correlates well with the shape and location of the salt-dome structure that was determined using 3D seismic prestack depth migration. The vertical cross

sections of the inverse image demonstrate reasonable recovery of the true geologic features.

We note that this result was obtained from relatively sparsely distributed marine MT test data collected in the Gemini prospect as early as 1997, 1998, 2001, and 2003. The modern MT surveys with the new generation of sea-bottom receivers and detailed areal coverage provide much better quality data than the Gemini data. The results of our study indicate that the application of the advanced large-scale 3D inversion methods to modern MT data has a potential to provide viable information about sea-bottom geologic formations, including salt structures.

ACKNOWLEDGMENTS

REFERENCES

Berdichevsky, M. N., and V. I. Dmitriev, 2002, Magnetotellurics in the context of the theory of ill-posed problems: SEG Investigations in Geophysics Series No. 11.

Blackford, L. S., J. Choi, A. Cleary, E. D'Azevedo, J. Demmel, I. Dhillon, J. Dongarra, et al., 1997, ScaLAPACK users' guide: Society for Industrial and Applied Mathematics.

Constable, S., K. Key, and L. Lewis, 2009, Mapping offshore sedimentary structure using electromagnetic methods and terrain effects in marine magnetotelluric data: Geophysical Journal International, **176**, no. 2, 431–442, doi: 10.1111/j.1365-246X.2008.03975.x.

Constable, S. C., A. S. Orange, G. M. Hoversten, and H. F. Morrison, 1998, Marine magnetotellurics for petroleum exploration: Part 1 — A sea-floor equipment system: Geophysics, **63**, 816–825, doi: 10.1190/1.1444393.

Cvetanovic, Z., 1987, Performance analysis of the FFT algorithm on a shared memory parallel architecture: IBM Journal of Research and Development, **31**, no. 4, 435–451, doi: 10.1147/rd.314.0435.

Ellingsrud, S., T. Eidesmo, S. Johansen, M. C. Sinha, L. M. MacGregor, and S. Constable, 2002, Remote sensing of hydrocarbon layers by seabed logging (SBL): Results from a cruise offshore Angola: The Leading Edge, **21**, 972–981, doi: 10.1190/1.1518433.

Gribenko, A., and M. S. Zhdanov, 2007, Rigorous 3D inversion of marine CSEM data based on the integral equation method: Geophysics, **72**, no. 2, WA73–WA84, doi: 10.1190/1.2435712.

Hoversten, G. M., S. C. Constable, and H. F. Morrison, 2000, Marine magnetotellurics for base-of-salt mapping: Gulf of Mexico field test at the Gemini structure: Geophysics, **65**, 1476–1488, doi: 10.1190/1.1444836.

Hoversten, G. M., H. F. Morrison, and S. Constable, 1998, Marine magnetotellurics for petroleum exploration: Part 2 — Numerical analysis of subsalt resolution: Geophysics, **63**, 826–840, doi: 10.1190/1.1444394.

Hursán, G., and M. S. Zhdanov, 2002, Contraction integral equation method in three-dimensional electromagnetic modeling: Radio Science, **37**, no. 6, 1089–1102, doi: 10.1029/2001RS002513.

Key, K. W., 2003, Application of broadband marine magnetotelluric exploration to a 3D salt structure and a fast-spreading ridge: Ph.D. thesis, University of California, San Diego.

Key, K. W., S. C. Constable, and C. J. Weiss, 2006, Mapping 3D salt using the 2D marine magnetotelluric method: Case study from Gemini Prospect, Gulf of Mexico: Geophysics, **71**, no. 1, B17–B27, doi: 10.1190/1.2168007.

Schuster, D. C., 1995, Deformation of allochthonous salt and evolution of related salt-structural systems, eastern Louisiana Gulf Coast, *in* M. P. A. Jackson, D. G. Roberts, and S. Snelson, eds., Salt tectonics: A global perspective: AAPG Memoir, **65**, 177–198.

Yoshioka, K., and M. S. Zhdanov, 2005, Electromagnetic forward modeling based on the integral equation method using parallel computers: 75th Annual International Meeting, SEG, Expanded Abstracts, 550–553.

Zhdanov, M. S., 2002, Geophysical inverse theory and regularization problems: Elsevier.

——, 2009, Geophysical electromagnetic theory and methods: Elsevier.

Zhdanov, M. S., and A. Gribenko, 2008, Joint three-dimensional inversion of magnetotelluric and magnetovariational data: 78th Annual International Meeting, SEG, Expanded Abstracts.

Zhdanov, M. S., A. Gribenko, and M. Čuma, 2007, Regularized focusing inversion of marine CSEM data using minimum vertical support stabilizer: 77th Annual International Meeting, SEG, Expanded Abstracts, 579–583.

Zhdanov, M. S., S. K. Lee, and K. Yoshioka, 2006, Integral equation method for 3D modeling of electromagnetic fields in complex structures with inhomogeneous background conductivity: Geophysics, **71**, no. 6, G333–G345, doi: 10.1190/1.2358403.

Zhdanov, M. S., L. Wan, A. Gribenko, M. Čuma, K. Key, and S. Constable, 2009, Rigorous 3D inversion of marine magnetotelluric data in the area with complex bathymetry: 79th Annual International Meeting, SEG, Expanded Abstracts, 729–733.